CLOUD IDENTIFICATION FOR ERBE RADIATIVE FLUX RETRIEVAL

by

Bruce A. Wielicki

and

Richard N. Green

Atmospheric Sciences Division

NASA Langley Research Center

Hampton, VA. 23665

For Submission to

Journal of Geophysical Research - Atmospheres

September 1987

(NASA-TM-101778) CLOUD IDENTIFICATION FOR FREE RADIATIVE FLUX RETRIEVAL (NASA. Langley Research Center) 52 p

N89-71110

Unclas

00/46 0213099

ABSTRACT

Global cloud cover conditions are commonly required for analyzing satellite data of relatively coarse spatial resolution such as the Nimbus 7 Earth Radiation Budget (ERB) measurements or the Earth Radiation Budget Experiment (ERBE) broadband scanner data. Cloud information is required so that measured broadband radiance at the satellite can be converted to an estimate of radiative flux at the top of the earth's atmosphere. The present paper discusses the application of a maximum likelihood estimation (MLE) technique to the problem of cloud cover determination for coarse resolution broadband satellite data. The technique uses empirical models for the angular dependence of radiance and is tested against simulated satellite observations. When used to determine cloud conditions for the inversion of satellite measured radiances to fluxes, the MLE approach shows substantial improvements over both a lambertian earth assumption and the clear/cloud threshold used in the inversion of Nimbus 3 and Nimbus 7 ERB scanner data. The MLE methodology will be used in the operational processing of the ERBE scanner data.

1. INTRODUCTION

The earth radiation budget has been estimated from satellite measurements since the launch of the Explorer 7 spacecraft in 1959 (House et al., 1986). The first measurements were made using instruments with a field of view encompassing the entire earth visible from the satellite. The attempt to obtain smaller spatial scale regional data began with the use of scanning radiometers on the TIROS satellites and was followed by Nimbus 2, Nimbus 3, Nimbus 6, Nimbus 7, and most recently the Earth Radiation Budget Experiment (ERBE). The smaller spatial field of view, however, necessitates a limited angular coverage for each scanner observation. In this case the direct measurement is radiance, while the desired measurement is radiative flux at the top of the atmosphere. Derivation of radiative flux using the scanner radiance observations then requires the use of angular dependence models (ADM's) to correct for the anisotropy of the radiation fields. To a large extent, the instantaneous accuracy of the estimated earth radiation budget is limited by the uncertainty in applying the ADM's (see Arking and Levine, 1967; Ruff et al., 1968; Raschke et al., 1973; Taylor and Stowe, 1984).

There are two major causes of variability in ADM's: change in geographic surface type (ocean, land, etc.) and change in cloud cover conditions (variable cloud cover and cloud 3-dimensional geometry). While surface conditions can in general be handled using a static geographic map, cloud conditions require dynamic identification of the scene being viewed in order to achieve accurate flux estimates.

The Nimbus 3 (N3) experiment (Raschke et al., 1973) made the first attempt to correct for the anisotropic character of the radiation emitted or reflected by the earth/atmosphere system. The N3 data were classified as viewing either ocean, land/cloud, or snow for shortwave correction. Longwave correction used two models, one for polar data (poleward of 70° latitude) and one for non-polar data. The five scene types selected were a result of limited data available to describe ADM's and of limited ability to distinguish clear from cloudy scenes.

As a result of the experience with the N3 data, the Nimbus 7 Earth Radiation Budget (N7-ERB) broadband scanner employed a bi-axial scan pattern which allowed the collection of data for a complete range of viewing zenith angle and viewing azimuth angles. These data were used to develop more complete ADM's over a wide range of scene types. Taylor and Stowe (1984) developed new ADM's using the N7-ERB data to construct bidirectional models for a range of uniform surface types; clear ocean, land, snow, ice and four altitude levels of overcast cloud. In order to derive these models, the N7-ERB shortwave and longwave radiances were sorted into each of the scene types. Surface type classification was derived by navigation of the data and subsequent comparison with a geographic map. Cloud cover was determined initially using the N7 Temperature-Humidity Infrared Radiometer (THIR) data. Four of these ADM's for ocean, land, cloud, and snow/ice were used in operational processing of the N7-ERB scanner data to produce broadband flux estimates (Jacobowitz et al., 1984). Cloud identification was performed for each ERB scanner field of view by setting thresholds to distinguish clear from cloud for both shortwave and longwave radiance. The thresholds were constant for all latitudes equatorward of 67.5° latitude and were independent of solar zenith angle, viewing zenith angle, and viewing azimuth angle. As shown by Arking and Vemury (1984) and Vemury et al. (1984), the simple threshold cloud/clear classification gives derived scanner shortwave reflected albedos which are larger than corresponding wide field of view shortwave albedos by several percent albedo. The primary cause of the discrepancy appears to be a substantial increase in the threshold determined cloud cover as satellite viewing zenith angle increases (Vemury et al., 1984).

A second concern is the use of only one cloud ADM derived using uniform overcast cloud conditions. Since directional reflectance patterns are a strong function of cloud geometry (Davies, 1984), it is likely that multi-level cloud systems or partial cloud cover conditions will give different ADM's than either clear or uniform overcast conditions. Davies' results also suggest that partial cloud cover directional patterns are not simply a linear combination of clear and overcast patterns.

In view of these concerns, the Earth Radiation Budget Experiment (ERBE) has chosen a bispectral cloud identification algorithm that uses broadband shortwave and longwave radiances simultaneously to select one of four cloud conditions (Smith et al., 1986). These four types are clear (0% - 5% cloud cover), partly-cloudy (5% - 50% cloud cover), mostly-cloudy (50% - 95% cloud cover), and overcast (95% - 100% cloud cover). A set of ADM's for each of these cloud conditions has been developed using the methodology described in Taylor and Stowe (1984) from N7-ERB data. Cloud identification for these new ADM's was improved over the earlier work by the incorporation of both THIR and TOMS data from the N7 satellite (Stowe et al., 1985). The TOMS measurement of solar reflected energy improves identification of low level clouds with small contrast in the thermal infrared THIR data.

Note that these cloud classes are based on cloud cover and not cloud height. There are two primary reasons for this selection. First, broadband radiances with 30 km or larger fields of view are inadequate to determine both cloud cover and cloud height categories simultaneously. Second, the primary purpose of the cloud identification is to select ADM's to correct radiance to flux. The largest corrections occur for shortwave ADM's as opposed to longwave ADM's or limb darkening models. These shortwave ADM's are dominated by changes in cloud cover (Davies, 1984) as opposed to cloud height, and the 3-dimensional broken cloud directional patterns discussed by Davies (1984) are implicitly included. Shortwave ADM's are also expected to vary with changes in cloud optical depth, and these effects are also included implicitly in the empirical ADM's. The ADM for each cloud cover category is then a composite for a range of cloud cover of all cloud height and cloud optical depths observed in the N7-ERB data set.

The ERBE will use a statistical approach to replace the constant thresholds used in previous radiation budget studies to distinguish clear from cloudy conditions. The approach taken is the use of a maximum likelihood estimator (MLE). The a priori data for this method are provided by the N7-ERB biaxial scanner and include both the ADM's and second order statistical moments. The ADM's and the statistics both are functions of viewing zenith angle, viewing azimuth angle (relative to the solar plane), and solar zenith angle. In the most general solution, a priori clear-sky regional fluxes are also used in the MLE algorithm.

Section 2 formulates the MLE algorithm, section 3 relates the algorithm to simpler threshold methods, section 4 presents an error analysis using simulated radiances, section 5 discusses the error analysis results, and section 6 gives summary conclusions.

2. Formulation of the Maximum Likelihood Estimator

The relation between flux M in Wm^{-2} and radiance ℓ in $Wm^{-2}sr^{-1}$ is given by the angular dependence model (ADM) definition

$$R(\theta,\phi,\theta_0) = \pi\, L(\theta,\phi,\theta_0)\, M^{-1} \tag{1a}$$

where R is the ADM value, θ is the viewing zenith angle of outgoing radiance L, θ_0 is the solar zenith angle, and ϕ is the viewing azimuth angle of L relative to the sun (see Smith et al., 1986, for further description of the angle definitions). Forward scatter is given by $\phi = 0$. A subscript "sw" is used to denote shortwave radiation at wavelengths less than 5μm (i.e. reflected solar radiation), and a subscript "lw" is used to denote longwave radiation at wavelengths greater than 5μm. Thus, the shortwave ADM or bidirectional model is denoted as R_{sw} and, from the definition given in (1a) has the normalization property

$$\pi^{-1} \int_{\phi=0}^{2\pi} \int_{\theta=0}^{\pi/2} R_{sw}(\theta,\phi,\theta_0) \cos\theta \sin\theta \, d\theta \, d\phi = 1 \tag{1b}$$

Similarly, the longwave ADM is R_{lw} and has normalization

$$2 \int_{\theta=0}^{\pi/2} R_{lw}(\theta,\xi) \cos\theta \sin\theta \, d\theta = 1 \tag{1c}$$

where ξ is colatitude. It follows from (1a) that an estimate of flux $\hat{M}$ at the top of the atmosphere (TOA) is given by

$$\hat{M} = \pi \, \ell \, R^{-1} \tag{2}$$

where ℓ is the measured radiance from satellite altitude. R varies, however, with both geographic surface type and cloud cover condition. Geographic surface type is determined using an a priori map. The purpose of the MLE algorithm is to classify cloudiness into one of four broad categories; clear, partly cloudy, mostly cloudy, or overcast. This scene identification selects the appropriate ADM used to convert a satellite measured radiance to an estimate of flux $\hat{M}$ at the TOA.

2.1 Algorithm definition.

The MLE algorithm requires a priori training data. In essence, it calculates from a priori data the expected satellite measurements for each of the four cloud cover conditions and identifies the one which is most likely in a statistical sense. Suppose the two broadband measurements are given by ℓ_{sw} and ℓ_{lw}. From the measurement location on the earth, the geographic surface type can be determined; and from a priori data, the mean clear-sky longwave flux M_{lw}^{clr} and the mean clear-sky overhead sun albedo a_0^{clr} of the viewed area can be determined. Thus, if the viewed area was clear, then the expected mean longwave measurement would be

$$L_{lw}^{clr} = \pi^{-1} R_{lw}^{clr}(\theta,\xi) \, M_{lw}^{clr} \tag{3a}$$

and the expected mean shortwave measurement would be

$$L_{sw}^{clr} = \pi^{-1} R_{sw}^{clr}(\theta,\phi,\theta_0) \, E_0 \cos\theta_0 \, \delta_{sw}^{clr}(\theta_0) \, a_0^{clr} \tag{3b}$$

where E_0 is the solar constant corrected to the earth-sun distance appropriate for the day of the observation, and $\delta_{sw}^{clr}(\theta_0)$ is the model representing the change in clear-sky albedo with solar zenith angle such that $a^{clr}(\theta_0) = a_0^{clr}\ \delta_{sw}^{clr}(\theta_0)$ and $\delta_{sw}^{clr}(\theta_0 = 0) = 1$. Moreover, there will be variation about these mean values which is modeled as a bivariate normal distribution. If we consider a small element $\Delta\ell_{sw}\Delta\ell_{lw}$ about the measurements, then the probability (or likelihood) that the pair of measured radiances were of a clear area is

$$\Pr[\ell_{sw},\ \ell_{lw} \text{ are clr}] = \Pr[\ell_{sw},\ \ell_{lw} |\ \text{clr}]\ \Pr[\text{clr}] \tag{4a}$$

where

$$\Pr[\ell_{sw}, \ell_{lw} |\ \text{clr}] = \frac{e^{-(Q/2)}\Delta\ell_{sw}\ \Delta\ell_{lw}}{2\pi\ \sigma_{sw}^{clr}\ \sigma_{lw}^{clr} \left[1 - (\rho^{clr})^2\right]^{1/2}} \tag{4b}$$

and

$$Q = \frac{1}{\left[1 - (\rho^{clr})^2\right]} \left[\left(\frac{\ell_{sw}^{clr} - L_{sw}^{clr}}{\sigma_{sw}^{clr}}\right)^2 - 2\ \rho^{clr} \left(\frac{\ell_{sw}^{clr} - L_{sw}^{clr}}{\sigma_{sw}^{clr}}\right) \left(\frac{\ell_{lw}^{clr} - L_{lw}^{clr}}{\sigma_{lw}^{clr}}\right) + \left(\frac{\ell_{lw}^{clr} - L_{lw}^{clr}}{\sigma_{lw}^{clr}}\right)^2 \right] \tag{4c}$$

The probability that the given surface type is clear Pr[clr], the standard deviations σ_{sw}^{clr}, σ_{lw}^{clr}, and the shortwave-longwave correlation coefficient ρ^{clr} have been defined from N7 data. The same procedure is followed to calculate Pr for partly cloudy, mostly cloudy, and overcast conditions. Finally, the cloud condition with the greatest probability of occurrence (i.e. the largest value of Pr) is chosen.

Figure 1 presents typical quantities for the four cloud conditions. The center points mark the mean (nominal) radiances, and the equiprobability ellipses illustrate the distribution. Note that partly cloudy scenes can exhibit the same shortwave and longwave radiances as mostly cloudy scenes. This is also true of the other scene types. The overlap is expected in view of the large variation in cloud optical depth and cloud height within each cloud cover type. The actual measurements are shown in Figure 1 by an "x." It is obvious that the MLE would identify this measurement pair as viewing a mostly cloudy area.

The conceptual drawing in Figure 1 can be compared to a bispectral histogram of the actual N7-ERB radiances as given in Figure 2 for a single viewing condition. The observations given in the histogram are for N7 scanner observations with solar zenith angles 53.1°-60.0°, viewing zenith angles 0°-15° and viewing azimuth angles 0°-180°. Each of the shortwave and longwave radiance pairs has been assigned a cloud condition based on auxiliary data from the THIR and TOMS instruments on the N7 satellite. These instruments have much smaller fields of view than the N7-ERB instrument and narrower spectral coverage, allowing more accurate cloud determination. A description of the cloud retrieval algorithm using THIR and TOMS data can be found in Stowe et al. (1985). Figure 2 demonstrates that the radiance distributions are roughly Gaussian in appearance and that there is substantial overlap in observed radiances as a function of cloud cover condition. Since two cloud conditions can exhibit the same measurements, the cloud condition cannot be defined deterministically, but must be defined statistically.

A problem arises with further consideration of the results given in Figure 2. Since the Nimbus 7 satellite has a sun-synchronous orbit with an equator crossing time near local noon, observations with a solar zenith angle near 56° will be taken in middle and high latitudes. The tropics will never be observed with a 56° solar zenith angle. This sampling limitation causes two difficulties. First, it is necessary to assume that the shortwave ADM's of all scene types are independent of latitude. Second, the longwave radiances given in Figure 2 would not be representative of tropical clear and cloudy emission. This second problem is alleviated by determining the longwave ADM's separately for each latitude zone. In general, longwave and shortwave ADM's might vary on a regional basis. The N7 orbit, however, limits the number of ADM's which can be developed. Shortwave ADM's are developed for 10 solar zenith ranges (every 0.10 in cosine of the solar zenith), and longwave ADM's are developed for 10 latitude zones (every 18° latitude). Longwave ADM's are further divided into four seasons of the year (Dec-Jan-Feb, Mar-Apr-May, Jun-Jul-Aug, and Sep-Oct-Nov).

The discussion above would treat a clear geographic surface type as having the same shortwave ADM and the same albedo independent of its location on the globe. Similarly, a clear geographic surface type would have the same longwave ADM and the same longwave flux independent of longitude within a single 18° latitude zone. An improvement to the MLE can be made by recognizing that geographic location provides information about expected clear-sky shortwave and longwave fluxes. For example, desert albedo may vary from 20% to 40% over different regions of the earth. If a single global desert albedo is used, brighter deserts will be perceived as having systematically higher cloud cover than darker desert regions. Similar arguments can be made concerning clear land albedo and longwave flux. Note that even though the N7-ERB sampling is insufficient to provide regional ADM's, regional clear-sky shortwave albedo and longwave flux can be estimated. Therefore, an additional set of desired a priori data are the nominal clear-sky longwave flux and the nominal clear-sky overhead-sun albedo values for all 2-1/2° regions over the earth. In order to utilize this clear-sky flux information in the MLE analysis, it is necessary to adjust the global partly cloudy, mostly cloudy, and overcast a priori fluxes to be consistent with the modified regional clear-sky fluxes.

For a given geographic scene type, let the global overhead-sun albedos for each cloud condition be denoted $\bar{a}_0^{clr}$, $\bar{a}_0^{pc}$, $\bar{a}_0^{mc}$, $\bar{a}_0^{ov}$ and the zonal mean longwave fluxes as $\bar{M}_{lw}^{clr}$, $\bar{M}_{lw}^{pc}$, $\bar{M}_{lw}^{mc}$, $\bar{M}_{lw}^{ov}$. Now the partly cloudy overhead-sun albedo for a given region a_0^{pc} is given by

$$a_0^{pc} = \bar{a}_0^{pc} + 0.75 \left[a_0^{clr} - \bar{a}_0^{clr} \right]. \qquad (5a)$$

The global quantity $\bar{a}_0^{pc}$ is adjusted to a regional quantity a_0^{pc} by adding 75% of the difference between the clear-sky regional albedo and the clear-sky global albedo. The 75% accounts for the fact that the partly cloudy scene is approximately 75% clear. The cloudy portion of the scene is assumed to be independent of the underlying surface albedo. This assumption is made in the absence of information concerning the behavior of broken clouds over variable reflectance backgrounds. Similarly, the mostly cloudy regional albedo is given by

$$a_0^{mc} = \bar{a}_0^{mc} + 0.25 \left[a_0^{clr} - \bar{a}_0^{clr} \right] \tag{5b}$$

and the overcast regional albedo by

$$a_0^{ov} = \bar{a}_0^{ov} \; . \tag{5c}$$

For variations within a latitude zone of regional clear-sky longwave flux, the conceptual model is that surface temperature changes regionally, but that the atmospheric temperature lapse rate and cloud height are constant. In this case, the difference between clear-sky and cloudy fluxes is approximately independent of changing clear-sky flux and

$$M_{lw}^{pc} = \bar{M}_{lw}^{pc} + \left[M_{lw}^{clr} - \bar{M}_{lw}^{clr} \right] \tag{6a}$$

$$M_{lw}^{mc} = \bar{M}_{lw}^{mc} + \left[M_{lw}^{clr} - \bar{M}_{lw}^{clr} \right] \tag{6b}$$

$$M_{lw}^{ov} = \bar{M}_{lw}^{ov} + \left[M_{lw}^{clr} - \bar{M}_{lw}^{clr} \right] \tag{6c}$$

where M_{lw}^{pc} is the regional longwave partly cloudy flux and $\bar{M}_{lw}^{pc}$ is the zonal longwave partly cloudy flux. Recall from (1) that while the shortwave ADM's are global in extent and vary with solar zenith angle, the longwave ADM's are independent of solar zenith angle but are defined for each of 10 latitude zones.

2.2 General example case

2.2.1 Description

Figure 3 gives an example of application of the MLE algorithm. The viewed area is ocean at the equator (0-18N latitude) during the northern hemisphere spring season (March-April-May). The clear sky conditions are $a_0^{clr} = 0.076$, $\delta^{clr} = 1.51$, and $M_{lw}^{clr} = 297.1\ Wm^{-2}$. The viewing geometry is $39° \le \theta \le 51°$, $53.1 \le \theta_0 \le 60$, and $60° \le \phi \le 90°$. Values for the different cloud conditions are given in Table 1. The lines drawn in Figure 3 show the decision boundaries between the four cloud conditions. At one point two of these boundaries intersect to form a triple point. The "+" characters mark the mean expected shortwave and longwave radiance for each cloud condition. Note that the majority of earth observations should fall along the lines joining the mean radiance points for the four cloud conditions. Except for the clear scene type, the boundaries along this line are approximately at the midpoints, but the boundaries are not perpendicular to the line. The slope of the boundary along the mean line is set by the ratio of the shortwave and longwave radiance standard deviations. An examination of Table 1 shows that the shortwave radiance standard deviations are much larger than the longwave radiance standard deviations. Further, the decision boundary between the clear and partly cloudy condition is very close to the mean clear radiance. This boundary is strongly affected by the large difference in a priori probability, that is $Pr[clr] = 0.05$ and $Pr[pc] = 0.46$. The relatively large a priori partly cloudy probability forces the decision boundary toward the mean clear radiance. It appears that on average, clear radiances as identified by the MLE will have larger longwave radiances and smaller shortwave radiances than the N7 a priori data.

2.2.2 Refinements

Further examination of the upper left corner of Figure 3 shows that it is possible for scenes which are warmer (large longwave radiance) and darker (small shortwave radiance) than clear-sky conditions to be classified as partly cloudy. This result can be seen by examining (4) and the radiance standard deviations in Table 1. Probability density decreases linearly with an increase in the product $\sigma_{sw}\ \sigma_{lw}$, but decreases exponentially with an increase in the product $[(\ell_{sw}-L_{sw})/\sigma_{sw}]\ [(\ell_{lw}-L_{lw})/\sigma_{lw}]$. Thus, observations ℓ_{sw},ℓ_{lw} which are several standard deviations away from the expected mean radiances for either cloud type will be identified as the cloud type with the largest standard deviation.

This artifact is caused by the fact that the radiance distributions of clear and partly cloudy scenes cannot be perfectly modeled as Gaussian. Even though this artifact will not occur often, it can be eliminated by application of thresholds beyond which clouds are not allowed to be chosen as the scene type. The dashed line in Figure 3 shows the clear-sky thresholds used in the MLE processing. Whenever both $\ell_{sw} < L_{sw}^{clr}$ and $\ell_{lw} > L_{lw}^{clr}$ the viewed area is defined as clear. Moreover, any radiance observations for which $\ell_{sw} < L_{sw}^{clr} - 2\sigma_{sw}^{clr}$ or $\ell_{lw} > L_{lw}^{clr} + 2\sigma_{lw}^{clr}$ are classified as clear.

There are two other restrictions on the MLE that improve the results. First, if the calculated probability of the most likely cloud condition is extremely small, then the validity of the measured radiances or the validity of the a priori data should be questioned. One way to implement this decision is to circularize the bivariate normal distribution of the identified scene type and require that the measurement be within N standard deviations from the mean values. The scene identification of measured radiances ℓ_{sw}, ℓ_{lw} is rejected if $d > N$, where

$$d = \left(\frac{\ell_{sw} - L_{sw}}{\sigma_{sw}}\right)^2 - 2\rho \left(\frac{\ell_{sw} - L_{sw}}{\sigma_{sw}}\right)\left(\frac{\ell_{lw} - L_{lw}}{\sigma_{lw}}\right) + \left(\frac{\ell_{lw} - L_{lw}}{\sigma_{lw}}\right)^2 . \quad (7)$$

Second, the identified scene should be questioned when the measured radiances have viewing angles in the forward scattering specular region. At this point the discrete ADM cannot accurately resolve the angular structure of reflectance, and large errors can result. This second restriction on the MLE is accomplished by setting a maximum shortwave anisotropic value of R^* and rejecting observations with $R > R^*$. A value of $R^* = 2$ is suggested, so that the scene identification is rejected when the expected shortwave radiance is twice that which would occur for a Lambertian reflector.

The MLE algorithm has been formulated as a bispectral algorithm using simultaneously measured shortwave and longwave radiances. For observations at night, however, the cloud condition must be identified using only longwave radiances. Similarly, if a longwave radiance is not available during the day (i.e. data dropout), then the cloud condition must be identified using only shortwave radiances. These cases are easily handled by eliminating the appropriate variable in the bivariate normal distribution (4). This change reduces the MLE to a 1-dimensional method.

3. Relationship of MLE to Simple Threshold Algorithms

The MLE algorithm can be simplified in several steps until the method becomes equivalent to simpler radiance threshold methods commonly employed in the detection of cloud cover. The steps to this simplification are instructive and are given in the discussion below. Results are given for the same example case presented in Figure 3.

3.1 Equal scene probability, Pr[k] = 0.25

Figure 4a gives the MLE scene selection boundaries for the case where the a priori scene probabilities Pr[k], k = clr, pc, mc, ov, are all set to 0.25. In this case the clear scene selection area in radiance space is increased, while that of partly cloudy is decreased relative to the general case.

3.2 Zero correlation, $\rho = 0$, and Pr[k] = 0.25

The effect of setting the correlation coefficient to zero in (4) is shown in Figure 4b. Along the line of mean radiances where most of the measurements will occur, the decision boundaries changed very little. The reason for this can be seen by examining the general form of the equiprobability ellipse given by

$$\left(\frac{x}{\sigma_x}\right)^2 - 2\rho_{xy}\left(\frac{x}{\sigma_x}\right)\left(\frac{y}{\sigma_y}\right) + \left(\frac{y}{\sigma_y}\right)^2 = \kappa^2. \qquad (8)$$

For simplicity we have assumed mean zero. The principle axes (x',y') of the ellipse are rotated from the xy axes by an angle Φ given by [Liebelt, 1967, p. 92]

$$\Phi = \frac{1}{2}\tan^{-1}\left[\frac{2\,\sigma_x\,\sigma_y\,\rho_{xy}}{\sigma_x^2 - \sigma_y^2}\right] \qquad (9)$$

and the principle variances are given by

$$\sigma_{x'}^2 = \sigma_x^2 \cos^2\Phi + 2\rho_{xy}\,\sigma_x\sigma_y \sin\Phi\cos\Phi + \sigma_y^2 \sin^2\Phi \qquad (10a)$$

$$\sigma_{y'}^2 = \sigma_x^2 \sin^2\Phi + 2\rho_{xy}\,\sigma_x\sigma_y \sin\Phi\cos\Phi + \sigma_y^2 \cos^2\Phi \qquad (10b)$$

If we set ρ_{xy} equal to zero, then $\Phi = 0°$ and the ellipse is aligned with the xy axes with principle variance of σ_x^2 and σ_y^2. These quantities have been determined from Table 1 for the general example problem and are given in Table 2. When the ratio σ_{sw}/σ_{1w} is large, the angle of rotation is small. In addition, the ratio of principle standard deviations shows that the shapes of the ellipses are not drastically altered. Thus, it is not surprising that the decision boundaries moved little when correlation was neglected.

3.3 <u>Equal variances, $\sigma_{sw}^k = \sigma_{1w}^k = \sigma$ for all k, $\rho = 0$, $\Pr[k] = 0.25$</u>

Now let us further simplify the MLE algorithm by setting the shortwave and longwave standard deviations to a constant σ for all four cloud conditions. In this case, the probability function (4) reduces to

$$\Pr[\ell_{sw}, \ell_{1w} | k] = \frac{1}{2\pi\sigma^2} \exp\left\{- \frac{1}{2\sigma^2}\left[\left(\ell_{sw} - L_{sw}^k\right)^2 + \left(\ell_{sw} - L_{sw}^k\right)^2\right]\right\} \Delta\ell_{sw}\Delta\ell_{1w} \qquad (11)$$

In this case maximizing the probability simplifies to minimizing simple distance in radiance space. Any radiance observation pair is classified as the cloud condition k which minimizes the distance

$$d = \left[\left(\ell_{sw} - L^{k}_{sw}\right)^{2} + \left(\ell_{sw} - L^{k}_{sw}\right)^{2} \right]^{1/2} \qquad (12)$$

between the a priori and measured radiances. Figure 4c gives the results of this simplification. Each decision boundary is simply the perpendicular bisector of a line drawn between two adjacent a priori mean radiance points. For measurements occurring along this line, the scene selection will be similar to the other cases considered. The net impact of this change on derived fluxes will be discussed in section 4.

3.4 One dimensional limit, $\sigma_{sw} >> \sigma_{lw}$, $\rho = 0$, $Pr[k] = 0.25$

In the limit as the shortwave standard deviation becomes large compared to the longwave standard deviation, the decision boundaries become horizontal lines and the scene identification is one dimensional. In this case there is little information content in the shortwave radiance measurement, resulting in use of the longwave radiance only. The decision boundaries are shown in Figure 4d and are typical of the case for scene identification for nighttime observations. The analogous case for $\sigma_{lw} >> \sigma_{sw}$ is shown in Figure 4e.

3.5 MLE simplified to N7-ERB scene identification algorithm

Having examined the simplifications of an MLE approach for cloud identification in sections 3.1 to 3.4, we can derive a set of simplifying conditions for which the MLE reduces to the N7 MATRIX cloud identification algorithm described by Jacobowitz et al (1982). The N7 MATRIX algorithm was used in the operational processing of the N7-ERB broadband data. The following conditions would simplify the MLE to the N7 algorithm:

1. Consider only clear and overcast cloud conditions.
2. Assume $\sigma_{lw}^{clr} = \sigma_{lw}^{ov} = \sigma_{lw}$ and $\sigma_{sw}^{clr} = \sigma_{sw}^{ov} = \sigma_{sw}$.
3. Assume $\sigma_{sw} \gg \sigma_{lw}$.
4. The average of clear and overcast mean longwave is 78.2 $Wm^{-2}sr^{-1}$, i.e. $(L_{lw}^{clr} + L_{lw}^{ov})/2 = 78.2$
5. Mean longwave radiances for clear and overcast cloud conditions do not vary with viewing zenith, measurement location on the earth, or time of year.

A final test is applied by the N7 MATRIX algorithm which is not used in the MLE approach. If the scene is selected as clear and the Lambertian albedo A calculated using the shortwave radiance measurement (i.e. $A = \pi L_{sw}/E_0\cos\theta_0$) is greater than a limit A_{max}, then the measurement is rejected. A_{max} for ocean background is 0.15 and A_{max} for land background is 0.50. The N7 scene identification algorithm result is shown in Figure 5 for comparison with the simplified versions of the MLE given in Figures 4a through 4e. Note that the rejection of data occurs for a substantial portion of the radiance space diagrams. The rejection area for the N7 MATRIX scene algorithm includes radiance values which the MLE algorithm would identify as partly cloudy, mostly cloudy and overcast, depending on the particular radiance values. The N7 data used to construct the statistics and ADM's for the MLE indicates that a significant portion of radiance data for this viewing condition will be rejected by the N7 MATRIX algorithm. We will return to this discrepancy and its impact on derived fluxes in section 4. This discrepancy points out the difficulty in applying global thresholds to classify scene types. At middle or high latitudes (lower longwave radiances), the region of rejected radiances would be outside the range of typical observations.

The Nimbus 3 scene selection algorithm (Raschke et al., 1973), was similar to the N7 MATRIX algorithm discussed above with a few differences: clouds and land are treated as the same scene type; and A_{max} is set to 0.10; the data rejected by the N7 MATRIX algorithm is classified as the cloud/land model (i.e. data with higher Lambertian albedo than A_{max} and higher longwave radiance than 78.2 $Wm^{-2}sr^{-1}$).

3.6 Variation of mean radiances with viewing angle.

Given the large variations in bidirectional reflectance found from the N7 data, we expect that the scene selection boundaries shown in Figure 3 would be strongly dependent on the viewing zenith angle, viewing azimuth angle, and solar zenith angle. Figure 6a gives an example of the variation of the mean radiances for all four cloud conditions over a wide range of viewing zenith angles at a fixed viewing azimuth angle (60°-90°) and fixed solar zenith angle (53°-60°). Figure 6b gives the same plot for an azimuth angle of 0-9 degrees (i.e. forward scattering). While small changes are found in Figure 6a, large differences are found in Figure 6b. Clearly, scene identification will vary with changing viewing zenith angle, especially for observations in the solar plane. Since this variation is a result of the anisotropy of the radiation reflected or emitted from the scene, correction of measured radiances to fluxes is also variable for the above viewing conditions.

3.7 Variation of mean radiances with latitude and season.

Figures 3 through 4e gave the MLE scene selection results for the case of tropical (0-18N latitude zone) conditions over an ocean background during spring (March-April-May). What happens for observations taken at higher latitudes? In this case, the expected longwave radiance will decrease for clear-sky conditions and may decrease or increase for overcast conditions. Figure 7 gives the variation of each of the four cloud scene types for the latitude zones from the equator to 72N latitude during the spring season (March-April-May) and for the same viewing angle conditions shown in Figure 3. Recall from section 2.1 that shortwave radiance values are independent of latitude. Figure 7 clearly shows large variations in the expected longwave radiance with latitude, consistent with the decrease in surface temperature from equator to pole. Since the latitudinal longwave radiance variation is much larger than the standard deviation of longwave radiance for clear-sky within a single latitude zone (approx. 3-5 $W/m^2/sr$ for ocean and 4-8 $W/m^2/sr$ for land), scene identification using an MLE approach should include the variation of longwave radiances with latitude. A similar argument would apply to seasonal temperature variations at middle and high latitudes. The MLE used to process ERBE data includes all of these effects.

4. Data Simulation

There are various modeling assumptions and error sources that affect the accuracy of the MLE algorithm. By simulating the satellite measured radiances, ℓ_{sw} and ℓ_{lw}, some of these assumptions can be evaluated. Specifically, the general example case and the simplified example cases discussed in section 3 will be simulated. Errors to be considered include both errors in identification of the scene type, and more importantly the resulting errors in derived shortwave and longwave flux.

The MLE solution for the general example problem is given in Figure 3. The concept used to perform the simulation experiment is to consider a set of measurement radiance pairs $(\ell^{i}_{sw}, \ell^{j}_{lw})$ which span the 2-dimensional radiance space shown in Fig. 3. The radiance space is sampled at discrete points i,j to minimize the computation required. The interval between radiance points is chosen as 1 W $m^{-2}sr^{-1}$. This value is chosen to be much less than one standard deviation in radiance for any cloud condition, but sufficiently large to minimize computational expense. For any pair of measurements $(\ell^{i}_{sw}, \ell^{j}_{lw})$ in radiance space, we can then identify the cloud condition K(i,j) as either clear, partly cloudy, mostly cloudy, or overcast. K is a cloud index taking on values 1 through 4 and specifies the ADM to be used for inverting the data. The resulting shortwave flux estimate at the TOA is from (2)

$$\hat{M}^{ij}_{sw} = \frac{\pi\, \ell^{i}_{sw}}{R^{K(i,j)}_{sw}} \tag{13}$$

where for a given i and j (i.e. shortwave and longwave radiance measurements), the MLE will determine a single value of K (i.e. scene type) as most likely. Next, compare this estimated flux with the true flux. For the purpose of simulation, we assume the distribution of measurements (i.e. Figure 2) can be exactly represented by four bivariate normal distributions with the parameters given in Table 1. In addition, the probability of occurrence of each cloud condition k is represented exactly by Pr[k] and the R values are true. Thus, the true mean flux at a point $(\ell^{i}_{sw}, \ell^{j}_{lw})$ will be a combination of the fluxes for each of the four scene types. Knowing the probability of occurrence of each scene type, the true mean shortwave flux for the point (i,j) in radiance space is given by

$$\bar{M}^{ij}_{sw} = \frac{\sum_{k=1}^{4} \omega^{ij}_{k} \, M^{ij}_{sw}(k)}{\sum_{k=1}^{4} \omega^{ij}_{k}} \tag{14a}$$

where from (2) $M^{ij}_{sw}(k) = \pi \, \ell^{i}_{sw} / R^{k}_{sw}$, and from (4)

$$\omega^{ij}_{k} = \Pr[\, \ell^{i}_{sw}, \ell^{j}_{lw} |\, k \,] \Pr[k] \tag{14b}$$

The flux error Δ^{ij}_{sw} is then the difference $\hat{M}^{ij}_{sw} - \bar{M}^{ij}_{sw}$ between the estimated flux and the true flux. Note that the true flux $\bar{M}^{ij}_{sw}$ is a statistical ensemble of all four cloud conditions which can occur for a given radiance measurement pair $(\ell^{i}_{sw}, \ell^{j}_{lw})$, while the estimated flux $\hat{M}^{ij}_{sw}$ is determined using the ADM appropriate only for the single cloud condition selected by the MLE.

Let us consider a grid of points $(\ell^{i}_{sw}, \ell^{j}_{lw})$ where $i=1,2,\ldots N_{sw}$ and $j=1,2,\ldots N_{lw}$ that cover the measurement space of Figure 3. At each combination of (i,j) the flux error is simulated. Finally, a weighted average of the flux errors over all points (i,j) is determined. The weight at each point $\Omega(i,j)$ is according to its probability of occurrence. The mean error for all possible radiance observations is then given by

$$\bar{\Delta}_{sw} = \sum_{i=1}^{N_{sw}} \sum_{j=1}^{N_{lw}} \Omega^{ij} \, \Delta^{ij}_{sw} \tag{15}$$

and the standard deviation of the flux error δ_{sw} is given by

$$\delta^2_{sw} = \sum_{i=1}^{N_{sw}} \sum_{j=1}^{N_{lw}} \Omega^{ij} \left[\Delta^{ij}_{sw} - \bar{\Delta}_{sw} \right]^2 \tag{16}$$

where

$$\Omega^{ij} = \sum_{k=1}^{4} \omega^{ij}_{k} \tag{17}$$

and the summation of Ω^{ij} over all i,j is equal to 1.0. The range of i,j used in the simulation covers only 99% of the expected radiance range so that a final normalization is necessary to adjust the sum of Ω^{ij} to 1.0.

The flux error derived above is the minimum error which the MLE methodology would produce given input data with the same statistics as the a priori data set. Note from (2) that if R^k_{sw} is the same for all scene types, then any cloud condition identified by the MLE would yield the correct flux. Also, if the four cloud types were sufficiently unique to avoid overlap in radiance space, then the MLE would always identify the correct scene and get zero error. Therefore, the simulation of the example problem determines flux errors which would result from the overlap between scene types and the associated change in anisotropy.

Table 3 gives results from simulations for all methodologies considered in section 3. Satellite viewing conditions are the same as those used for Figures 3 and 4. Given in Table 3 are both the fraction of simulated satellite observations classified as each of the four cloud conditions, and the errors in estimated shortwave and longwave fluxes at the TOA. Simulation of the general example gave cloud condition percentages that were very close to the a priori values. The shortwave flux estimate is biased by

1 Wm^{-2} and the standard deviation of the error is 5.6 Wm^{-2}. The longwave flux estimates are very good, with mean zero and a standard deviation of 0.1 Wm^{-2}. This later result is expected in view of the small changes in R^k_{lw} for the four cloud conditions. Further discussion of this result is given in section 6. The use of equal scene a priori probabilities (section 3.1) affect the clear and partly cloudy frequencies but have little effect on flux errors. Also the effect of eliminating correlation (section 3.2) is small. The equal standard deviations case (section 3.3) increases the shortwave flux errors but has little effect on the longwave fluxes. When the scene is identified using only the longwave radiances, large increases in shortwave error are found. When the scene is identified using only the shortwave radiances, the standard deviation of shortwave error increases substantially. The N7 scene identification algorithm caused large errors in both shortwave and longwave fluxes. The longwave bias error results from the region of rejected radiance observations which rejects many of the large longwave flux observations and thereby biases the mean longwave flux estimate too low. The shortwave error is a combination of this effect and the use of only a clear and overcast shortwave anisotropic model. If the radiances in the N7 rejected area are classified as overcast, then $\bar{\Delta}_{sw}=$ -4.9 Wm^{-2} and $\bar{\Delta}_{lw}=$ 0.4 Wm^{-2}. Finally, the result of applying Lambertian anisotropic models (i.e. $R = 1.0$, or $\hat{M} = \pi \ell$) gives errors an order of magnitude larger than the other methods.

Although the simulations are presented for only one sampling condition, other conditions have been simulated. The errors shown are neither the largest nor the smallest of those found for other viewing conditions. Unfortunately, there is no single meaningful error which can be quoted. Satellite viewing geometry will vary greatly over different regions of the earth, different times of day, and different satellite orbits. Work is in progress to derive more general results using N7-ERB data by applying the MLE algorithm and then comparing to the Sorting into Angular Bins (SAB) method of Arking and Vemury (1984) over the entire earth for the month of June 1979.

5. Discussion

Section 4 discussed the magnitude of derived TOA flux errors using an MLE approach to identify the cloud condition. To a great extent, these errors represent the ambiguity of the relationship between shortwave and longwave radiance and the scene types to be classified. Figures 1 and 2 showed the substantial overlap between adjacent scene types. If the overlap did not occur, the flux errors given in Table 3 would have been zero. If the flux errors are caused by ambiguous cloud type selection, then another strategy to evaluate fluxes would be to utilize an anisotropic factor R for any given observation which weighted the R value for each scene type by the probability that the observed radiances came from that scene type. For example, if the observed radiances fell on the MLE decision boundary between the clear and partly cloudy scene types, a composite of the two anisotropic models could be used. While the results are not presented here, this approach was found to give similar flux errors to those for the general MLE approach. Since discrete scene types are simpler to implement and interpret, the general MLE approach was chosen.

5.1 Shortwave flux errors

If overlap or ambiguity is the major source of error in the theoretical error analysis results, it would follow that increasing the number of cloud conditions might eliminate much of the ambiguity. Unfortunately, substantial overlap of cloud conditions in radiance space is likely to be inevitable whenever the existence of partial cloud cover in a single observation is a common occurrence. For shortwave radiance, the ambiguity is caused by the variability of cloud albedo, cloud fraction, and cloud bidirectional reflectance. As an example of the large variability of cloud conditions, reconsider the data shown in Table 1. If clouds exhibited uniform albedo and uniform bidirectional reflectance, then the standard deviation of shortwave radiance for a given viewing condition would result only from the allowed range of cloud cover in the overcast category of 95% to 100% cloud cover. The standard deviation of shortwave radiance should then be less than 2% of the mean shortwave radiance. The ratio σ_{sw}/L_{sw} from Table 1 is 25.3% for overcast conditions, much greater than 2%. Evidently most of this variability is caused by fluctuations in cloud albedo and bidirectional reflectance. The ratio σ_{sw}/L_{sw} for the mostly cloudy condition is 41.9%, even larger. At first, the larger variability for the mostly cloudy cloud condition would seem to be caused by the larger variation in cloud cover allowed in this cloud class (50% - 95%). A uniform distribution of cloud cover from 50% to 95%, however, would only give a (0.29)(95-50) = 13% value of σ_{sw}/L_{sw} if albedo and bidirectional reflectance were held fixed. Instead, it is likely that the variation of bidirectional reflectance is dominating the partial cloud cover conditions, especially in view of the highly variable cloud geometry and cloud optical depth likely to occur for these conditions. Unfortunately, the number of N7 observations was judged insufficient to produce cloud bidirectional reflectance models for smaller intervals of cloud cover. A topic for further research is to establish the amount of decrease in radiance variability which can be achieved by examining smaller cloud cover intervals and by examining additional classes of cloud type, such as cloud height, aspect ratio, and optical depth.

5.2 Longwave flux errors

The overlap between scene types in longwave radiance is caused by the variation of cloud height, cloud emissivity, cloud fraction, and cloud longwave ADM (i.e. limb-darkening). The cloud fraction classes currently defined give ADM's which vary by only 1% to 2% between the various scene types. In this case, any error in scene selection causes only small errors in derived TOA longwave flux. The similarity of the longwave ADM's was not anticipated. Most cloud models treat clouds as plane-parallel and optically thick (i.e. black) in the infrared. This conceptual model would predict that longwave ADM's should become increasingly isotropic as cloud cover increases. In fact, the overcast category has similar limb-darkening to the clear, partly cloudy, and mostly cloudy scene types. This result is probably traceable to two effects. First, optically thin cirrus cloud is strongly limb-darkened. Second, broken 3-dimensional cloud fields increase limb-darkening relative to that of plane-parallel cloud fields (Naber and Weinman, 1984; Duvel and Kandel, 1984). The longwave errors given in the simulation are likely to substantially underestimate the true standard deviation of error in TOA longwave flux. Additional cloud categories for cloud height and cloud emissivity would be required to more accurately derive longwave fluxes.

6. Conclusions

An improved methodology for identifying cloud conditions has been developed for use in studies of the earth's radiation budget. This maximum likelihood estimation (MLE) methodology has been developed in concert with new models of the anisotropy of the earth's outgoing radiation field and improves the accuracy of the flux estimates at the top of the atmosphere using broadband radiance measurements. For this reason the MLE has been chosen for use by the Earth Radiation Budget Experiment (ERBE) data processing system. The MLE is a bispectral identification algorithm that uses measured shortwave and longwave broadband radiances to identify the cloud type. This identification depends on the viewing zenith angle, the viewing azimuth angle, the solar zenith angle, the 2.5° latitude/longitude region observed, and season. A substantial amount of a priori data is required, including angular dependence models and their statistics for all scene types. The geographic scene type (land, ocean, desert, etc.) of each 2.5° region is defined along with a mean regional clear-sky overhead sun albedo. These overhead sun albedoes are corrected to the observation sun condition using models of albedo variation with solar zenith. These a priori data are then used to compute an expected mean radiance from each of four cloud conditions and a statistical "distance" measure selects the cloud condition with the maximum likelihood. Thus, the MLE identifies the satellite measurement as observing either a clear scene, partly cloudy scene, mostly cloudy scene, or an overcast scene.

When compared to the use of a lambertian assumption, simulations indicate that the MLE methodology can reduce bias errors in derived fluxes by more than a factor of 10. The standard deviation of error is reduced by more than a factor of 5. The methodology gives a factor of 2 to 3 improvement over the simpler threshold methodologies previously employed in the analysis of Nimbus 3 and Nimbus 7 earth radiation budget data. Since the simulation error analysis requires assumptions about the statistics of the earth's radiation field, further validation of the methodology is recommended using analysis of the ERBE and N7 data. The simulations provide initial lower limits on the errors.

While the primary purpose of the MLE approach is to select the appropriate angular dependence model, a crude measure of cloud amount is generated as a by-product. This product is potentially useful as an initial analysis tool for the separate determination of cloudy and clear radiative properties. Ultimately, however, a more accurate determination of cloud radiative properties will require the combined analysis of the ERBE and International Satellite Cloud Climatology Project (ISCCP) data.

Acknowledgments. This work is indebted to the development of improved angular dependence models by V. Ray Taylor and Larry L. Stowe at NOAA, National Earth Satellite Service. Their work was a necessary precursor to the present paper. This work also benefited from many discussions with members of the ERBE Science Team, especially Tim Suttles, Lou Smith, Jim Coakley, Pat Minnis, Lee Avis, Ed Harrison, Bruce Barkstrom, Ray Taylor, and Larry Stowe. Discussions with Sastri Vemury also improved the present work.

REFERENCES

Arking, A. and J. Levine, Earth albedo measurements: July 1963 to June 1964, J. Atmos. Sci., 24, 721-724, 1967.

Arking, A. and S. Vemury, The NIMBUS 7 ERB data set, a critical analysis, J. Geophys. Res., 89, 5089-5097, 1984.

Davies, R., Reflected solar radiances from broken cloud scenes and the interpretation of scanner measurements, J. Geophys. Res., 89, 1259-1266, 1984.

Duvel, J. P. and R. S. Kandel, Anisotropy of longwave radiation emergent from a broken cloud field and its effect on satellite estimates of flux, J. Clim. Appl. Met., 23, 1413-1420, 1984.

House, F. B., A. Gruber, G. E. Hunt, and A. T. Mecherikunnel, History of satellite missions and measurements of the earth radiation budget (1957-1984), Rev. Geophys., 24, 357-377, 1986.

Jacobowitz, H., H. V. Soule, H. L. Kyle, F. B. House, and the Nimbus 7 ERB Experiment Team, The earth radiation budget (ERB) experiment: An overview, J. Geophys. Res., 89, 5021-5038, 1984.

Liebelt, P. B., An introduction to optimal estimation, Addison-Wesley Pub., 273pp, 1967.

Naber, P. S. and J. A. Weinman, The angular distribution of infrared radiances emerging from broken fields of cumulus clouds, J. Geophys. Res., 89, 1249-1257, 1984.

Raschke, E., T. H. Vonder Haar, M. Pasternak, and W. R. Bandeen, The radiation balance of the earth-atmosphere system from Nimbus-3 radiation measurements, NASA TN D-7249, 73pp, 1973. (NTIS N7321702)

Ruff, I. R., R. Koffler, S. Fritz, J. S. Winston, and P. K. Rao, Angular distribution of solar radiation reflected from clouds as determined from TIROS-IV radiation measurements, J. Atmos. Sci., 25, 323-332, 1968.

Smith, G. L., R. N. Green, E. Raschke, L. M. Avis, J. T. Suttles, B. A. Wielicki, and R. Davies, Inversion methods for satellite studies of the earth's radiation budget: Development of algorithms for the ERBE mission, Rev. Geophys., 24, 407-421, 1986.

Stowe, L. L., P. P. Pellegrino, P. H. Hwang, P. K. Bhartia, T. F. Eck, C. G. Wellemeyer, S. M. Read, and C. S. Long, Validation of Nimbus-7 cloud products, Proc. Intn'l. Rad. Symp., A. Deepak Pub., 228-231, 1985.

Taylor, V. R. and L. L. Stowe, Reflectance characteristics of uniform earth and cloud surfaces derived from NIMBUS-7 ERB, J. Geophys. Res., 89, 4987-4996, 1984.

Vemury, S. K., L. Stowe and H. Jacobowitz, Sample size and scene identification (cloud): Effect on albedo, J. Geophys. Res., 89, 5345-5353, 1984.

FIGURE CAPTIONS

Figure 1. Conceptual drawing of equiprobability ellipses for each of the four scene types: clear ocean (clr), partly cloudy ocean (pc), mostly cloudy ocean (mc), and overcast (ov). Mean radiances for each scene type are marked by a "+". Example observation is marked by an "x".

Figure 2. Bispectral histogram of the Nimbus 7 ERB broadband radiances used to construct angular dependence models (ADM's) and statistics used by the MLE scene identification algorithm. Observations are for solar zenith angles 53.1°-60.0°, viewing zenith angle 0°-15°, and all viewing azimuth angles. Observations include all latitude zones.

Figure 3. General example case of MLE scene selection algorithm. Mean radiances for each scene type are marked by a "+". Solid lines give the decision boundaries between the different scene types. Observations with radiances above or to the left of the dashed line are classified as clear (i.e. very large longwave radiance or very low shortwave radiance). Results given are for latitude zone 0-18N, solar zenith angles 53.1°-60°, viewing zenith angle 39°-51°, viewing azimuth angles 60°-90° and season March-April-May.

Figure 4a. Simplification of the case in Figure 3 assuming equal a priori probabilities of all scene types.

Figure 4b. Simplification of the case in Figure 3 assuming zero correlation coefficient and equal a priori probability for all four scene types.

Figure 4c. Simplification of the case in Figure 3 assuming equal radiance variance, zero correlation coefficient and equal a priori probability for all four scene types.

Figure 4d. Simplification of the case in Figure 3 assuming the variance of shortwave radiance is much greater than the variance of longwave radiance and assuming equal a priori probabilities.

Figure 4e. Simplification of the case in Figure 3 assuming the variance of longwave radiance is much greater than the variance of shortwave radiance and assuming equal a priori probabilities.

Figure 5. Application of the N7-ERB scene identification algorithm to the case in Figure 3. The mean radiances used by the MLE are given by a "+" for reference with the previous figures.

Figure 6a. Variation of mean shortwave and longwave radiances for each scene type as a function of viewing zenith angle for solar zenith angle 53.1°-60°, viewing azimuth angle 60°-90° and season March-April-May.

Figure 6b. Variation of mean shortwave and longwave radiances for each scene type as a function of viewing zenith angle for solar zenith angle 53.1°-60°, viewing azimuth angle 0°-9° and season March-April-May.

Figure 7. Variation of mean shortwave and longwave radiances for each scene type as a function of latitude for solar zenith angle 53.1°-60°, viewing zenith angle 39°-51°, viewing azimuth angle 60°-90° and season March-April-May.

TABLE 1. Radiance Statistics for the Example in Figure 3

Cloud Condition	Apriori Prob.	Shortwave Radiance	Shortwave Std. Dev.	Longwave Radiance	Longwave Std. Dev	Correl. Coef.	Shortwave Anisotropy	Longwave Anisotropy
Clear	0.05	16.46	3.6	95.89	3.4	-0.221	0.599	1.014
P. Cloudy	0.46	31.48	12.7	92.33	4.1	-0.366	0.712	1.014
M. Cloudy	0.28	68.77	28.8	79.73	8.5	-0.451	0.872	1.015
Overcast	0.21	109.81	27.8	60.29	15.5	-0.545	0.919	1.011

TABLE 2. Impact of Correlation Coefficients on the Radiance Statistics Given in Table 1.

Cloud Condition	σ_{sw}/σ_{lw}	Φ (degrees)	σ'_{sw}/σ_{sw}	σ'_{lw}/σ_{lw}
Clear	1.06	-37.0	1.077	0.905
P. Cloudy	3.12	-7.3	1.007	0.923
M. Cloudy	3.37	-8.2	1.009	0.884
Overcast	1.79	-20.7	1.056	0.793

TABLE 3. Cloud Conditions and TOA Fluxes vs. the NIMBUS 7 Reference Values.

	CLOUD CONDITIONS (%)				FLUX ERRORS (W/m^2)			
METHODOLOGY	CLEAR	PCLDY	MCLDY	OVCST	$\overline{\Delta}_{sw}$	δ_{sw}	$\overline{\Delta}_{lw}$	δ_{lw}
N7: THIR/TOMS REFERENCE	5.0	46.0	28.0	21.0	N/A	N/A	N/A	N/A
MLE: GENERAL	3.7	51.2	28.0	17.1	1.0	5.6	0.0	0.1
MLE: EQUAL SCENE PROBABILITY	14.9	37.9	27.8	19.4	1.4	6.9	0.0	0.1
MLE: CORR. COEF. = 0	14.7	39.2	26.6	19.5	1.6	7.1	0.0	0.2
MLE: EQUAL STD. DEV.	18.8	37.1	22.4	21.6	2.0	9.8	0.0	0.2
MLE: LONGWAVE ONLY	26.2	27.2	29.2	17.4	7.2	20.5	0.0	0.2
MLE: SHORTWAVE ONLY	16.8	37.8	22.9	22.5	1.1	10.8	0.0	0.2
N7 MATRIX: REJECT NOT USED	36.0	0.0	0.0	31.2	4.4	15.8	-8.7	0.3
N7 MATRIX: REJECT = CLEAR	68.8	0.0	0.0	31.2	28.6	51.4	0.1	0.3
N7 MATRIX: REJECT = OVCST	36.0	0.0	0.0	64.0	-4.9	22.0	0.4	0.6
LAMBERTIAN	N/A	N/A	N/A	N/A	-36.6	37.0	3.5	3.6

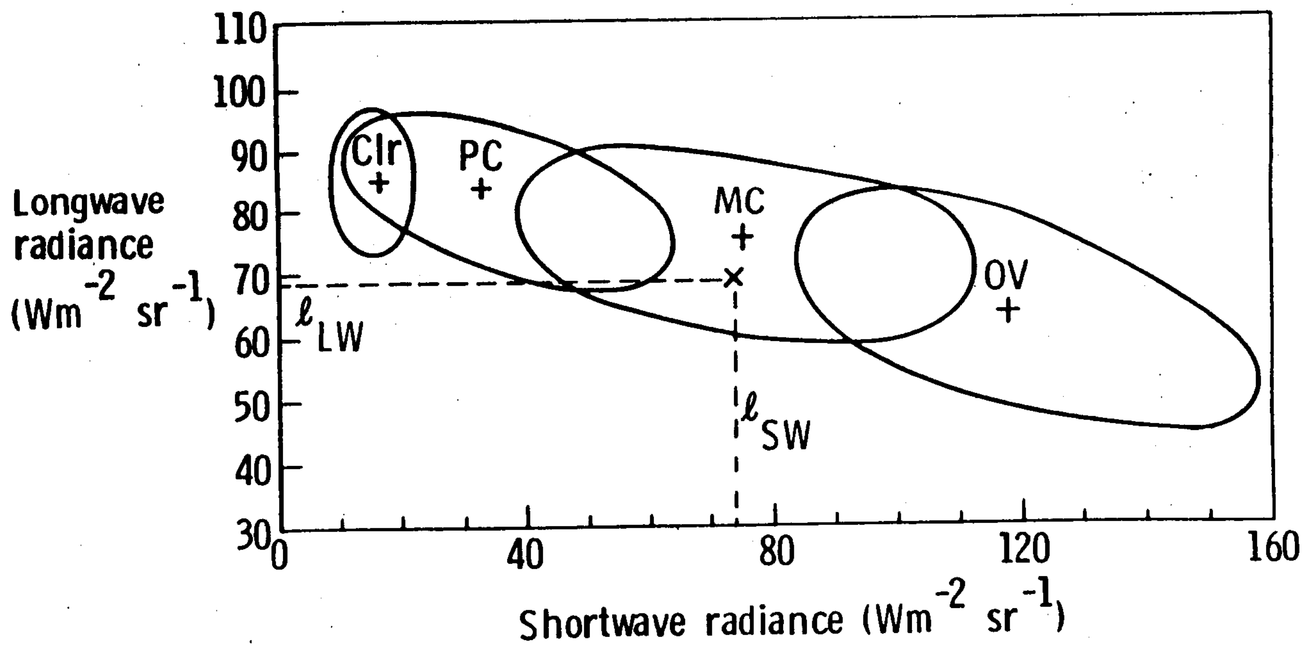
110
100
90
80
70
60
50
40
30
0
40
80
120
160
Longwave radiance (Wm^{-2} sr^{-1})
Shortwave radiance (Wm^{-2} sr^{-1})
Clr
PC
MC
OV
ℓ_{LW}
ℓ_{SW}

FIGURE 1

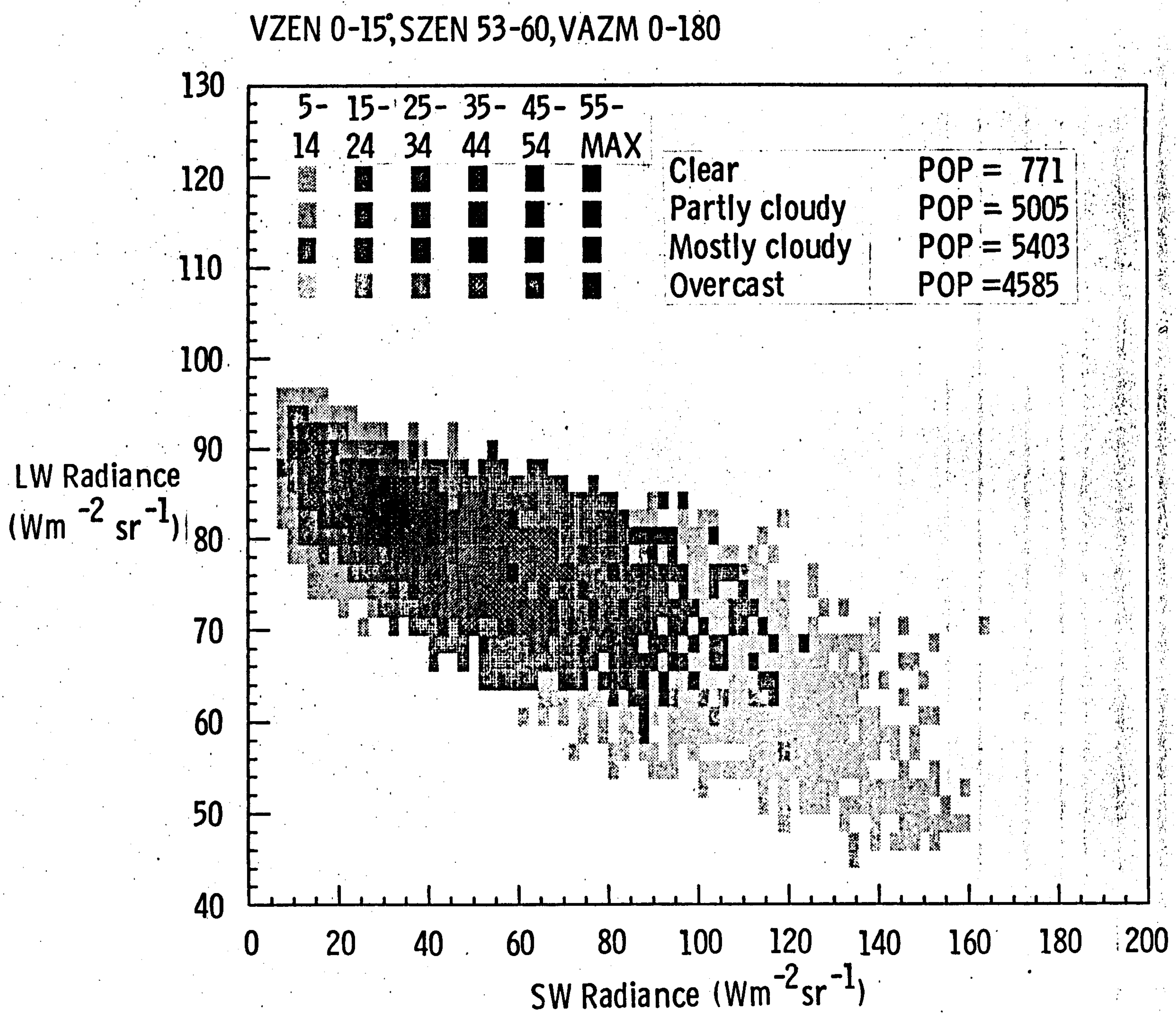
VZEN 0-15°, SZEN 53-60, VAZM 0-180
5-14
15-24
25-34
35-44
45-54
55-MAX
Clear POP = 771
Partly cloudy POP = 5005
Mostly cloudy POP = 5403
Overcast POP =4585
LW Radiance (Wm^{-2} sr^{-1})
130
120
110
100
90
80
70
60
50
40
0
20
40
60
80
100
120
140
160
180
200
SW Radiance (Wm^{-2}sr^{-1})

FIGURE 2

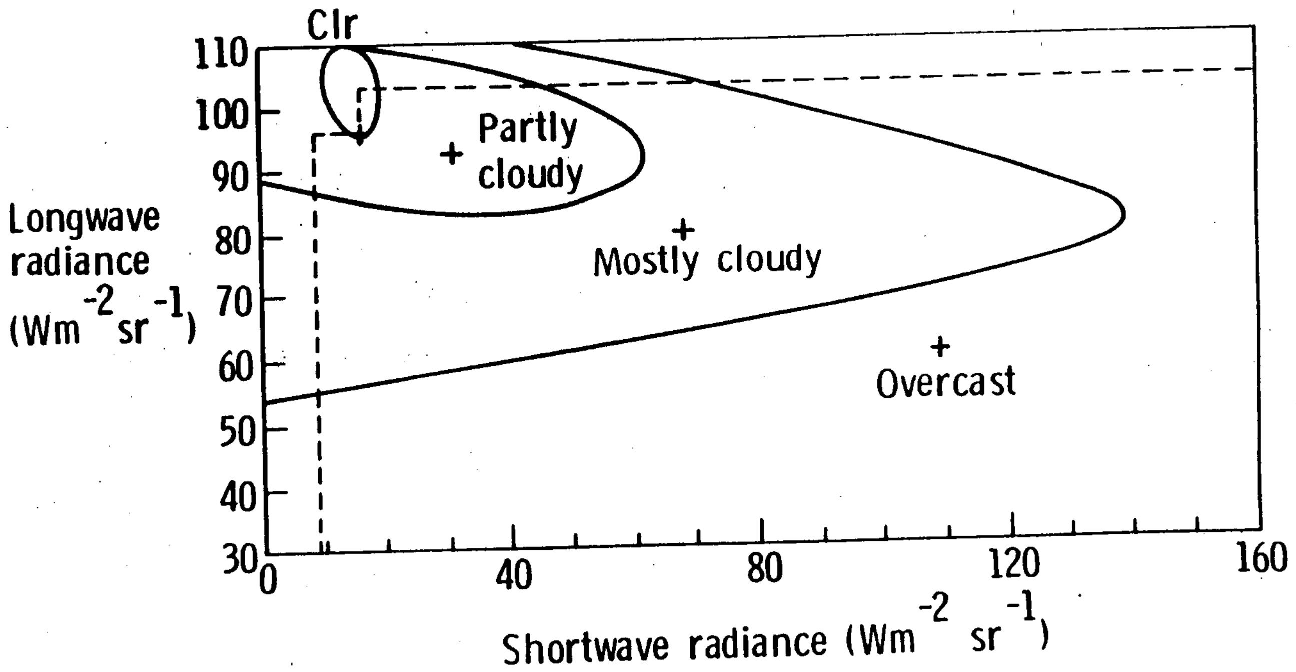
GENERAL CASE

FIGURE 3

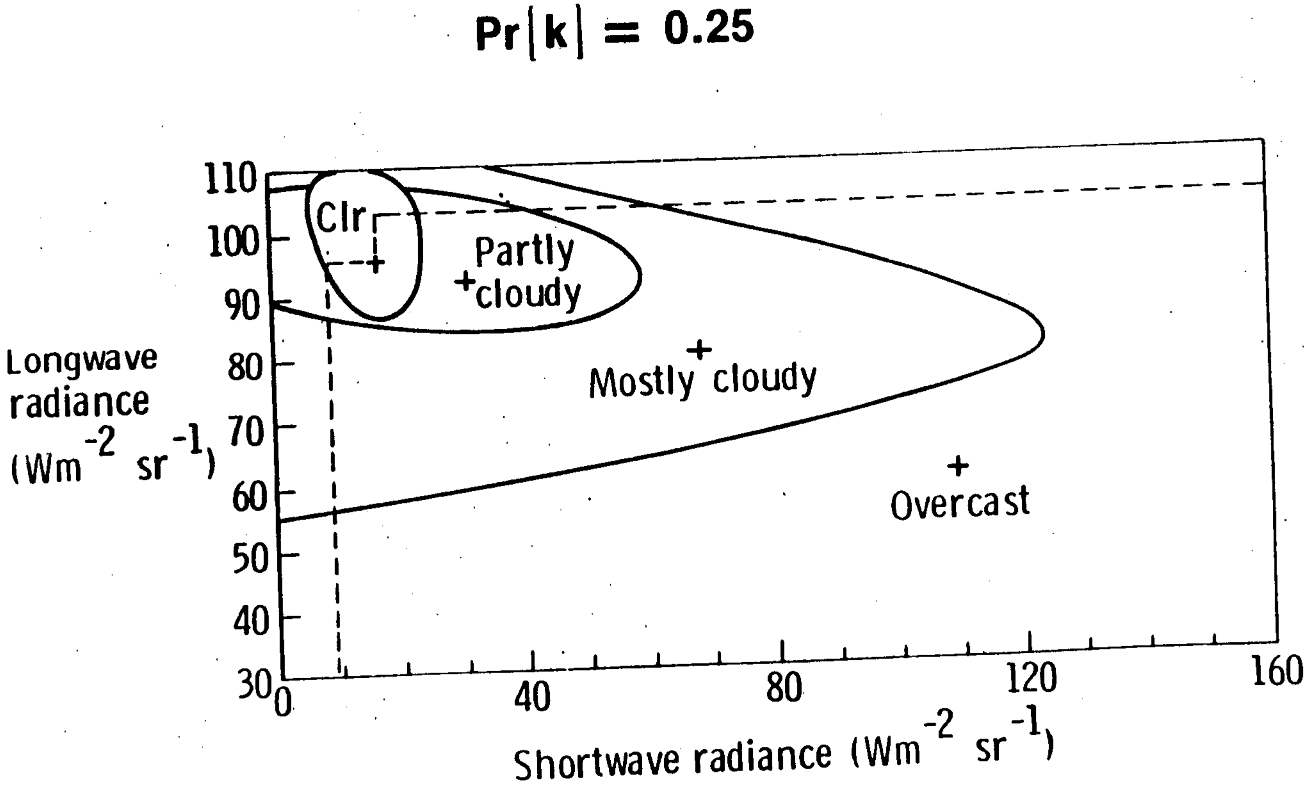

$Pr|k| = 0.25$

FIGURE 4A

$Pr|k| = 0.25, \rho|k| = 0.0$

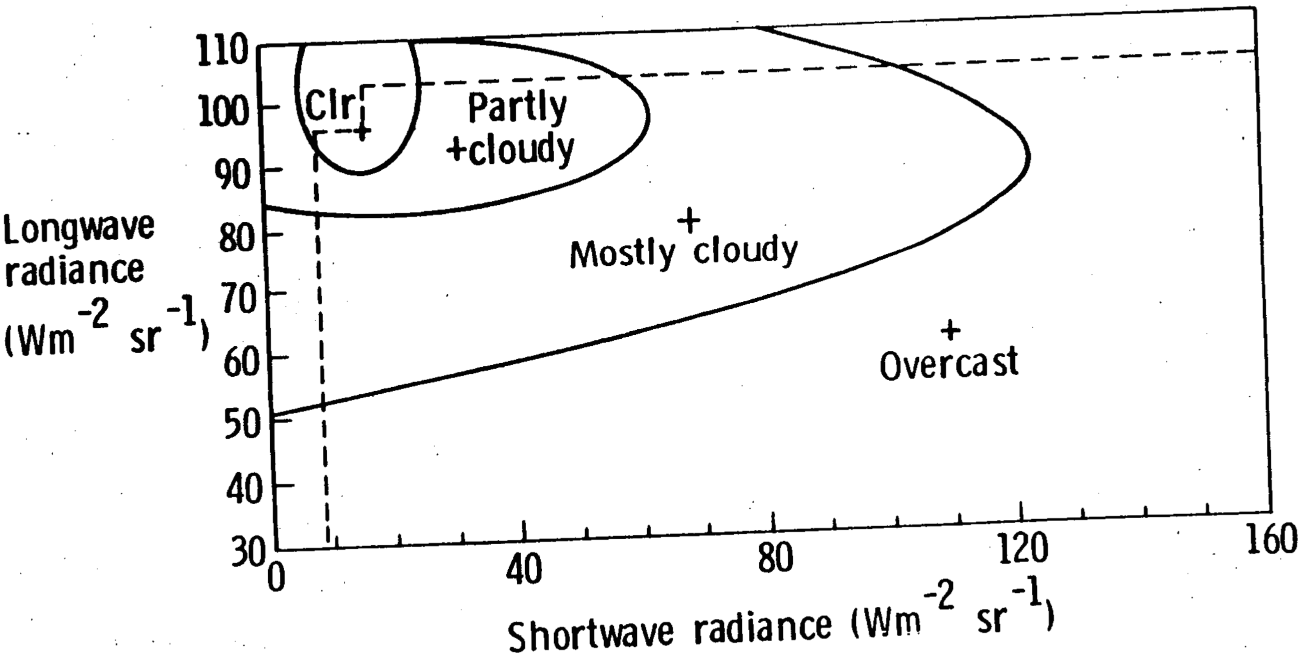

FIGURE 4B

$\Pr[k] = 0.25,\ \rho[k] = 0.0,\ \sigma_{SW}[k] = \sigma_{LW}[k] = \sigma$

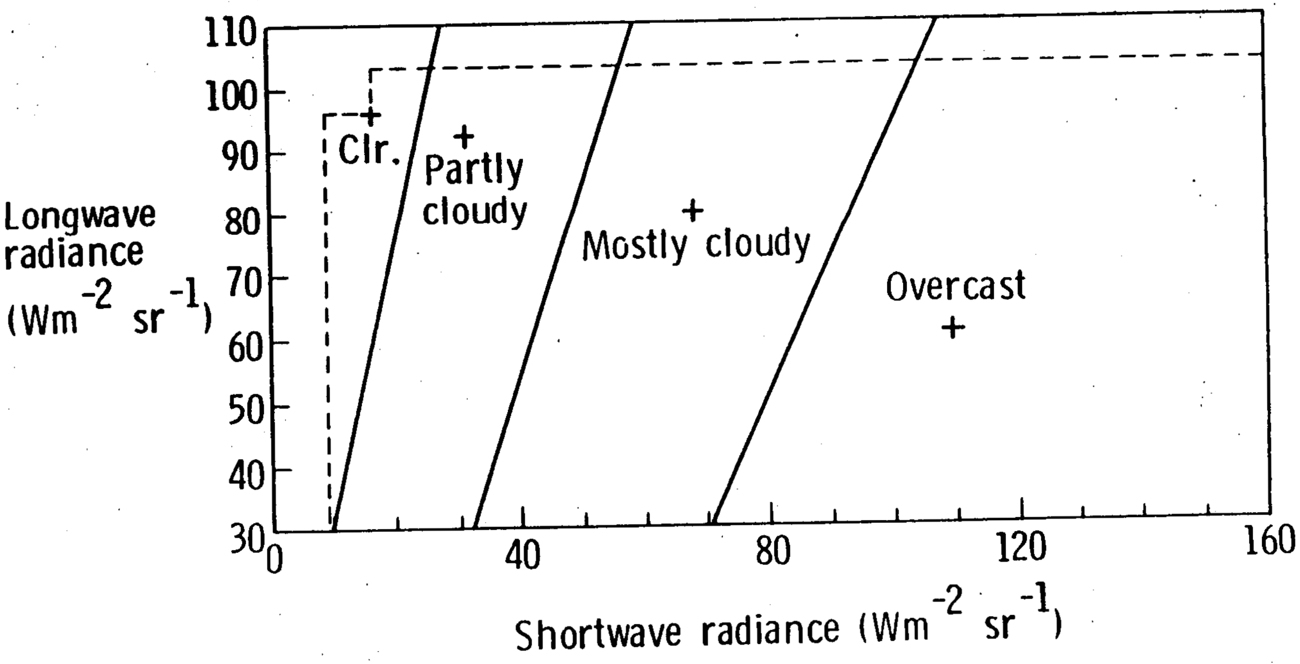

FIGURE 4c

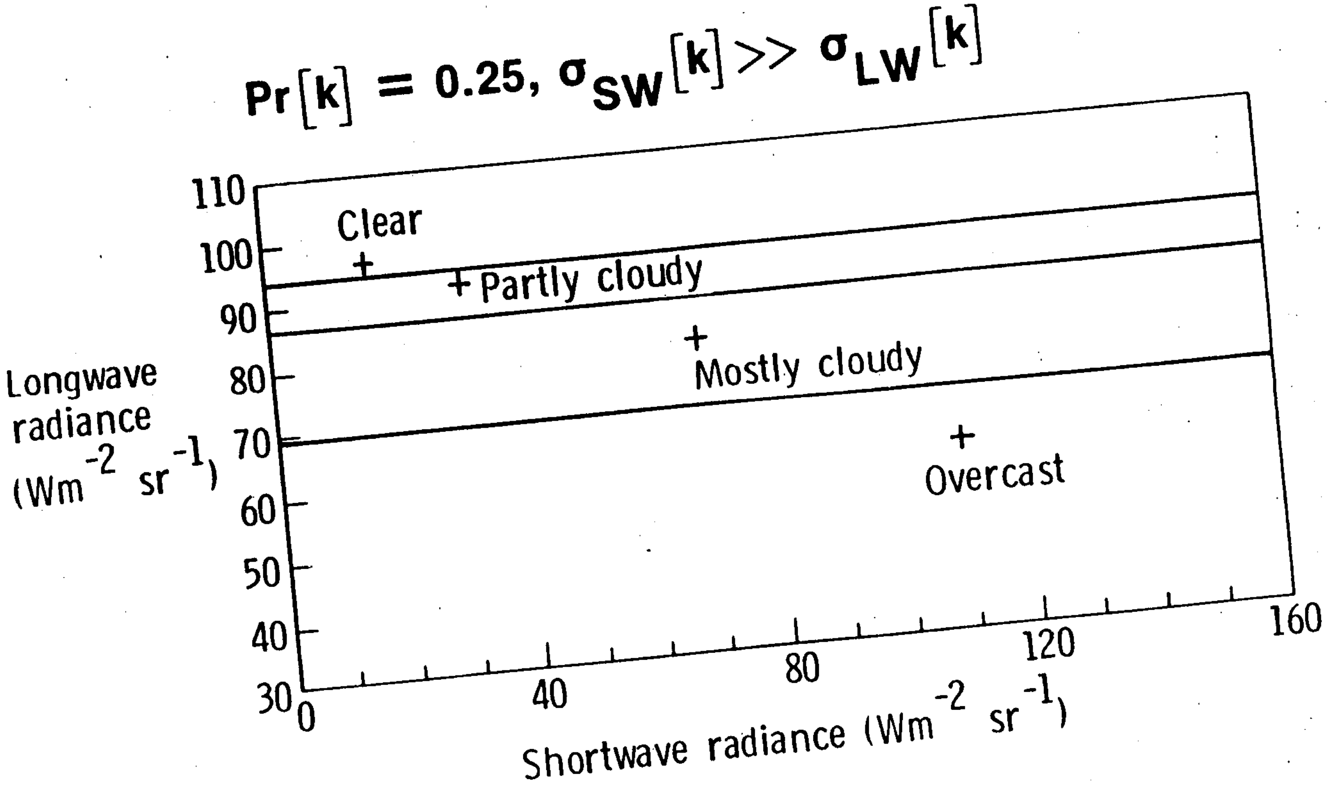

$Pr[k] = 0.25, \sigma_{SW}[k] >> \sigma_{LW}[k]$

FIGURE 4D

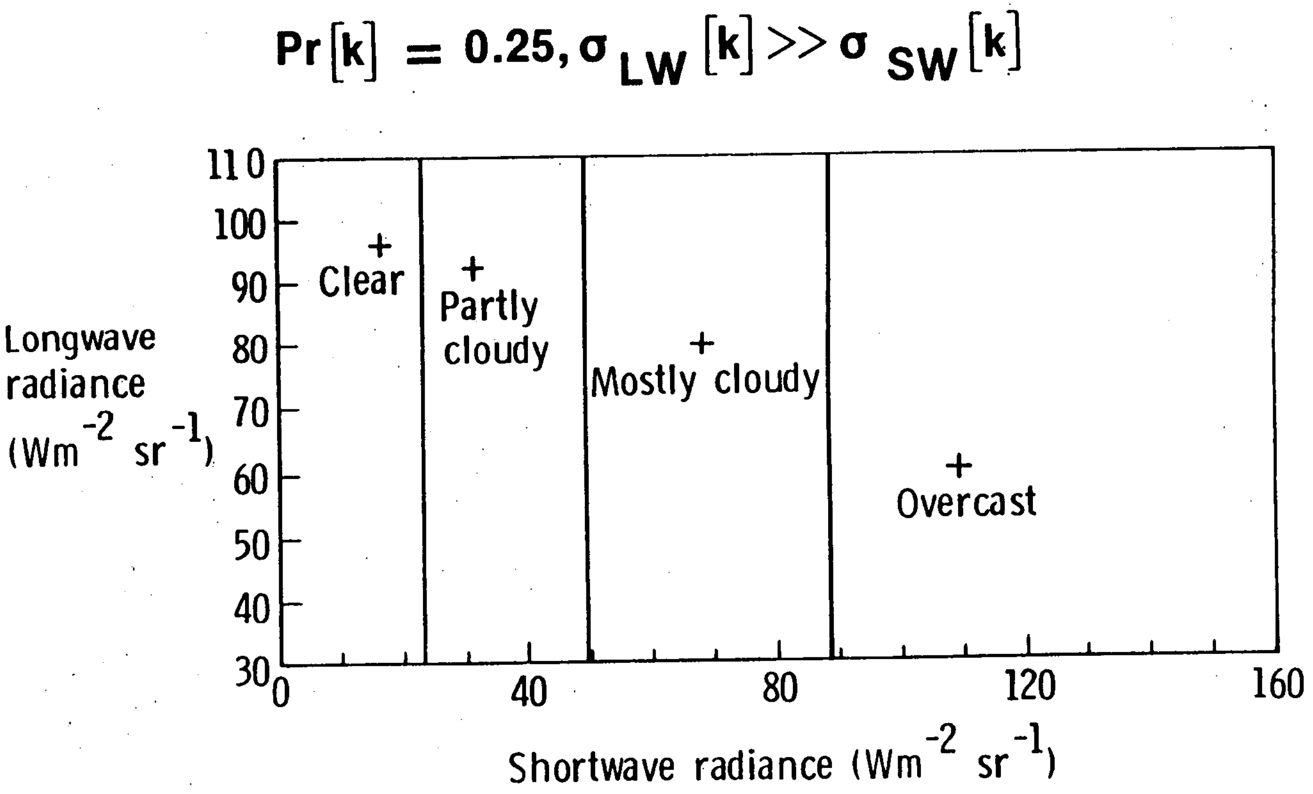
$Pr[k] = 0.25, \sigma_{LW}[k] >> \sigma_{SW}[k]$
Longwave radiance ($Wm^{-2}\ sr^{-1}$)
110
100
90
80
70
60
50
40
30
0
40
80
120
160
Shortwave radiance ($Wm^{-2}\ sr^{-1}$)
Clear
Partly cloudy
Mostly cloudy
Overcast

FIGURE 4E

NIMBUS 7 MATRIX ALGORITHM

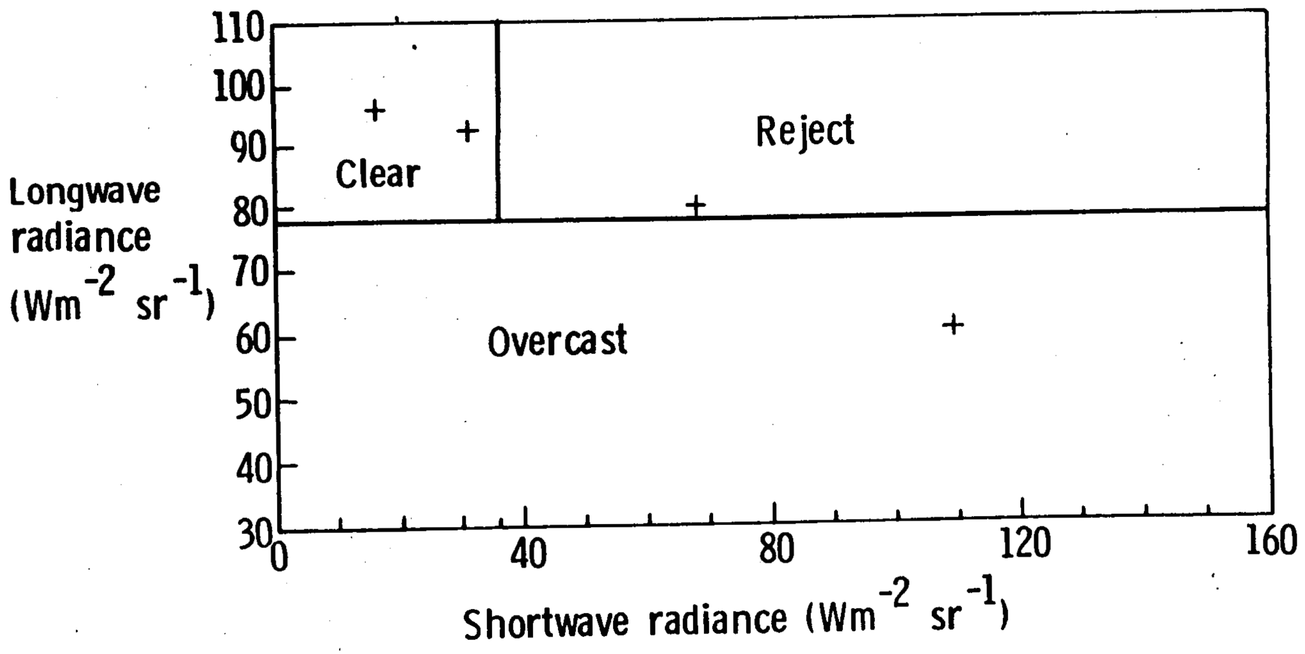

FIGURE 5

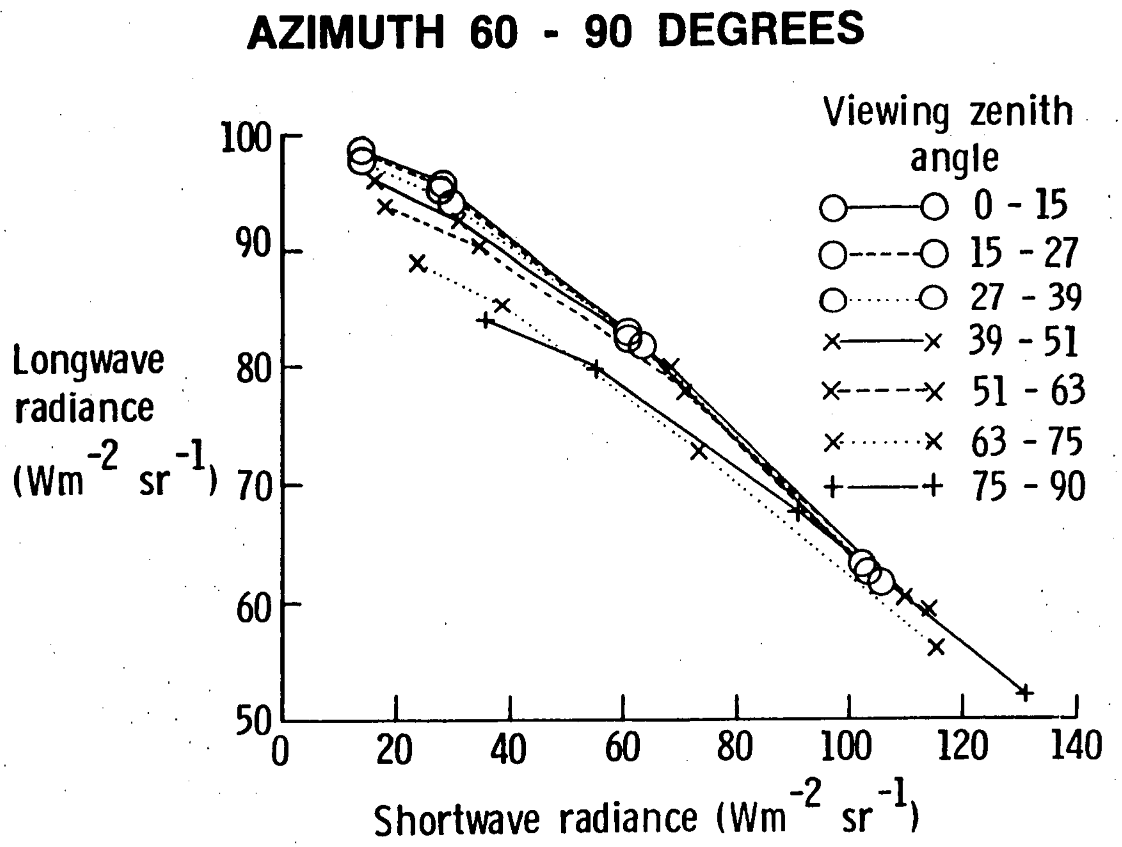
AZIMUTH 60 - 90 DEGREES
Viewing zenith angle
0 - 15
15 - 27
27 - 39
39 - 51
51 - 63
63 - 75
75 - 90
Longwave radiance (Wm^{-2} sr^{-1})
100
90
80
70
60
50
0
20
40
60
80
100
120
140
Shortwave radiance (Wm^{-2} sr^{-1})

FIGURE 6A

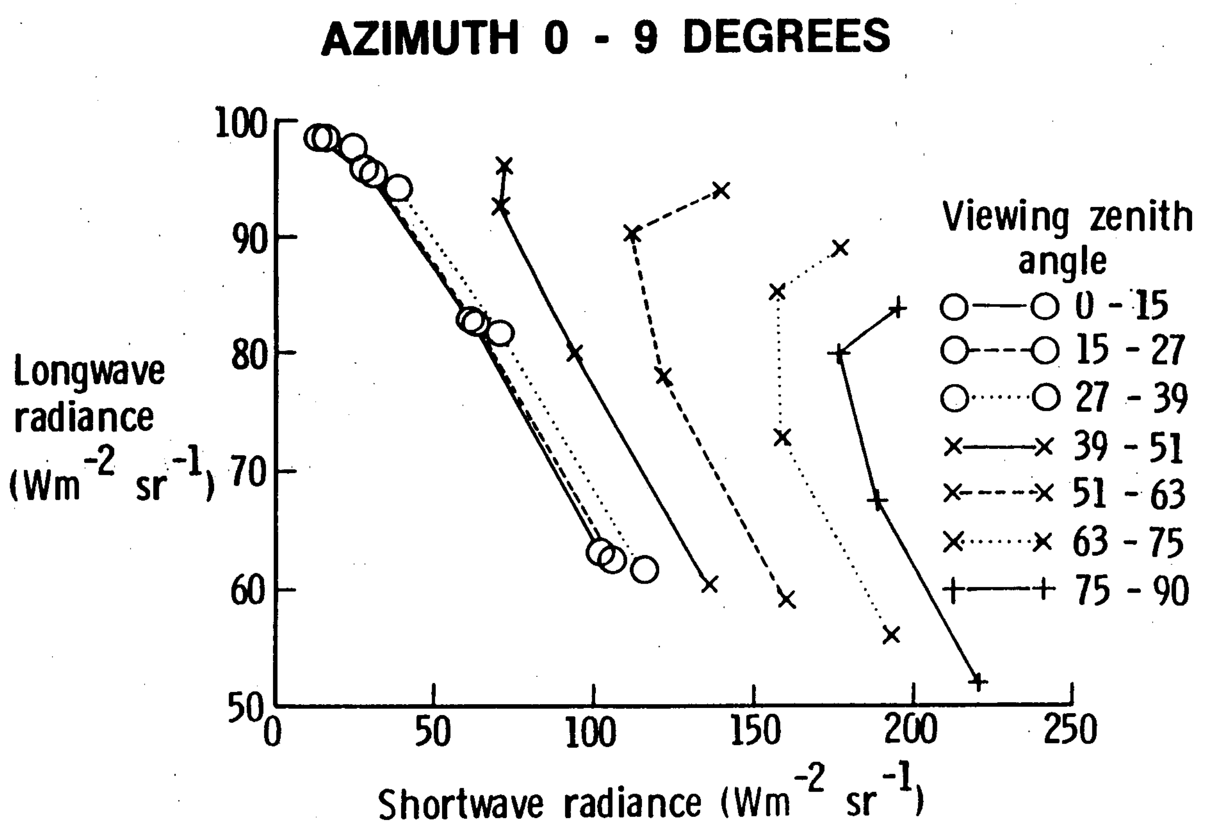
AZIMUTH 0 - 9 DEGREES
Longwave radiance $(Wm^{-2}\ sr^{-1})$
100
90
80
70
60
50
0
50
100
150
200
250
Shortwave radiance $(Wm^{-2}\ sr^{-1})$
Viewing zenith angle
0 - 15
15 - 27
27 - 39
39 - 51
51 - 63
63 - 75
75 - 90

FIGURE 6B

S. ZENITH 53.1° - 60°, V. ZENITH 39° - 51°, V. AZIMUTH 60° - 90°

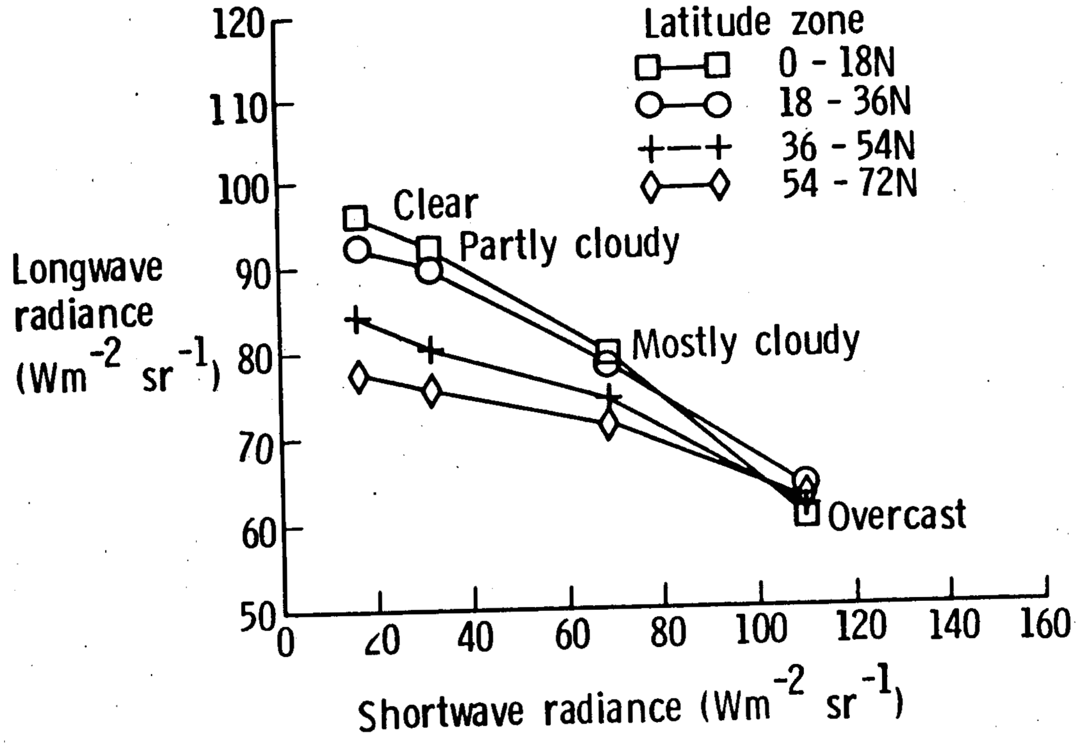

FIGURE 7